Biophysical Journal, Volume *119*

Supplemental Information

Infrared Excitation Induces Heating and Calcium Microdomain Hyperactivity in Cortical Astrocytes

Elke Schmidt and Martin Oheim

Supplementary Information

Pulse-length effects in 2P-micoscopy. I. Infrared excitation induces brain heating and calcium microdomain hyper-activity in cortical astrocytes

Elke Schmidt[a] and Martin Oheim[a *, ✉]

[a]Université de Paris, SPPIN – Saints Pères Paris Institute for the Neurosciences, CNRS, Paris, F-75006 France.

*ORCID id: orcid.org/0000-0001-8139-167X

✉ martin.oheim@parisdescartes.fr

This PDF file includes:

Supplementary text
Figs. S1 to S6
Table S1
Captions for movies S1 to S2
References for SI reference citations

Other supplementary materials for this manuscript include the following:

Movies S1 to S2

SUPPLEMENTARY TEXT

List of abbreviations

2P	-	two-photon
4-OH	-	4-hydroxy (-tamoxifen)
ACSF	-	artificial cerebrospinal fluid
AOM	-	acousto-optical modulator
a.u.	-	arbitrary units
Ca^{2+}	-	calcium
CNRS	-	*Centre National de la Recherche Scientifique*
DAPI	-	4',6-Diamidine-2'-phenylindole dihydrochloride
EU	-	European Union
GDD	-	group delay dispersion
i.p.	-	intraperitoneally
IP_3R2	-	inositol 1,4,5-trisphosphate receptor subtype2
GUI	-	graphical user interface
KO	-	knock-out
OCT	-	optimal cutting temperature
OD	-	optical density
PBS	-	phosphate buffered saline
PCR	-	polymerase chain reaction
PFA	-	paraformaldehyde
ROI	-	region of interest
SD	-	standard deviation
SEM	-	standard error of the mean

SUPPLEMENTAL ONLINE METHODS

Drugs and reagents

Unless otherwise stated, reagents were purchased from Sigma Aldrich (Deisenhofen, Germany).

Immunofluorescence

Mice were anesthetized with pentobarbital, injected *i.p*. (150 mg/kg body weight), perfused with 4% paraformaldehyde (PFA) in 0.02M phosphate buffered saline (PBS) and their brains were removed, postfixed in PFA (2h, 4%) and cryoprotected in 20% sucrose in 0.02 M PBS overnight. Tissue was frozen in Optimal Cutting Temperature (OCT) compound (Sakura Finetek Europe, Leiden, Netherlands) at -30° for cutting 16-µm sections with a cryostat. Sections were stored at -80°C prior to use. For immunofluorescence, slides were defrosted, washed 2× 15 min in 0.02 M PBS, and incubated overnight with primary antibodies (see Table S1) diluted in 0.02 M PBS, 0.02% Na-azide, 0.3 M Triton X-100 at room temperature (RT, 20-23°C) in a humid chamber. The day after, slides were washed 4× 15 min in 0.02M PBS, and incubated 2h with the secondary antibody diluted in 0.02 M PBS, 0.02% Na-azide, 0.3M Triton X-100 (see Table S1). Finally, slides were washed 2× in PBS (15 min, 0.02 M), mounted with Vectashield (containing DAPI, Vector Laboratories, Burlingame CA, USA), and sealed with coverslips. Slices incubated with secondary antibodies only were used as negative controls to set parameters for antibody-specific fluorescence image acquisition in each experiment. Images were acquired in epifluorescence (Axio Observer Z1, ZEISS, Oberkochen, Germany) fitted with a PlanNeoFluar ×20/0.5-NA objective, a COLIBRI-2 4-LED light-source (365 nm, 470 nm, 590 nm, 625 nm) and matched ZEISS filter cubes (see details in Table S1). Identical acquisition settings were used for the negative controls and experimental slides.

SUPPLEMENTARY FIGURES

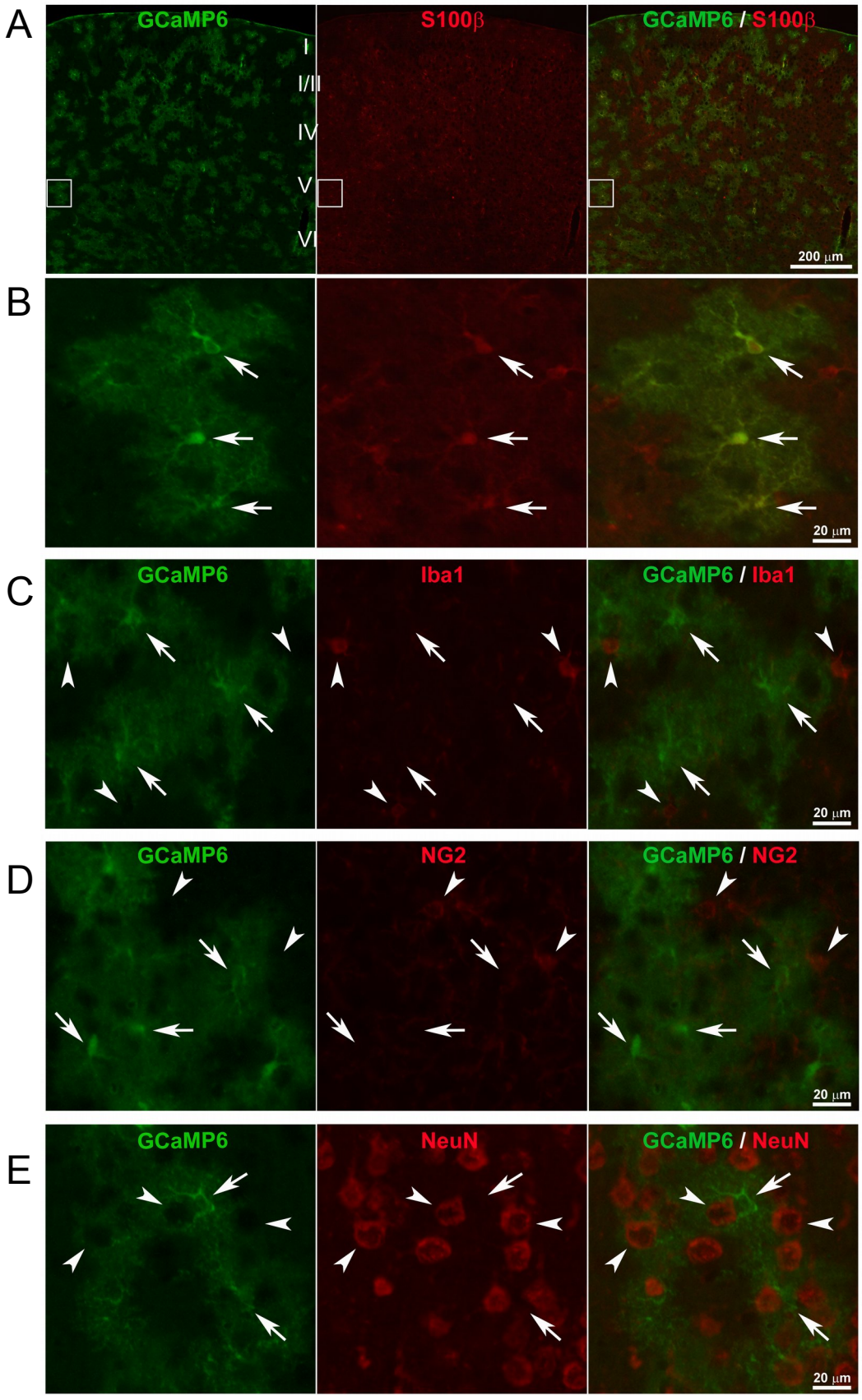

Fig. S1. GLAST-driven GCaMP6f expression is astrocyte-specific.

Immunofluorescence imaging of slices from GLAST-CreER^{T2}::GCaMP6f mice. (*A*) Throughout layers I-VI of the somatosensory cortex of 4-OH tamoxifen-injected mice, the genetically encoded Ca^{2+} indicator GCaMP6f (*top*, *left*) was selectively expressed in S100β-positive astrocytes (*top*, *middle*). Some 42% of S100β^{+} astrocytes expressed GCaMP6f and 99% of GCaMP6f^{+} cells expressed S100β. (*B*) Pseudo-color red-green overlap (*right*) at the single-cell level (*arrows* mark astrocyte cell bodies) when zooming in on the boxed region in (A). GCaMP6f is neither expressed in Iba1-positive microglia (C, *arrowheads*) nor in NG2-expressing oligodendrocyte precursor cells (D), and only marginal expression is detected in NeuN-positive neurons (<0.05%, panel E). Scale bars: 200 and 20 μm, respectively, as shown on the rightmost panel.

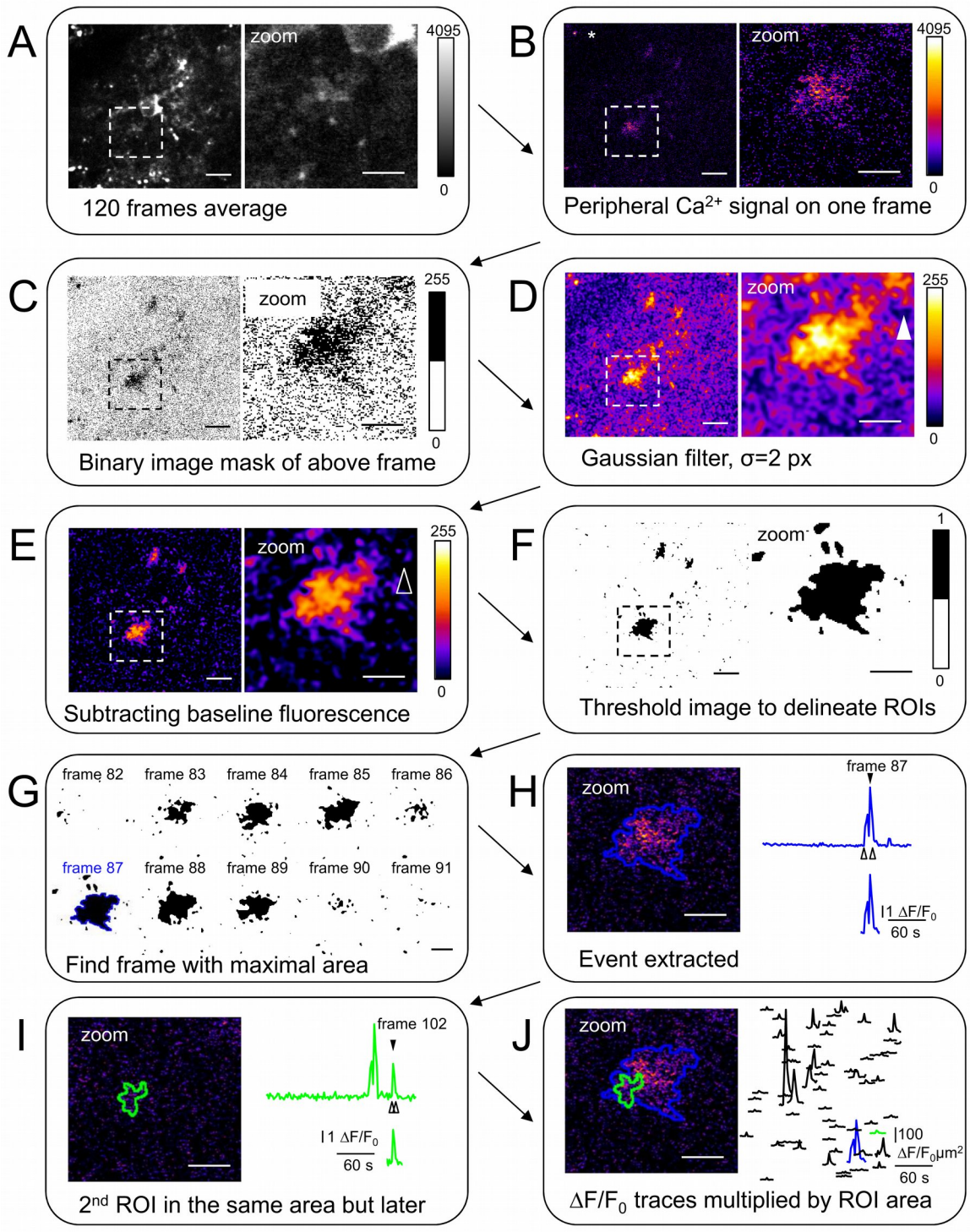

Fig.S2 ImageJ and IGOR routine for ROI- and event-detection. Steps of semi-auto-mated detection of Ca^{2+} transients in astrocyte processes. (*A*) Time-average of an 2P-fluorescence image series (0.5 Hz, 120 frames) recorded in a GLAST-creER^{T2}:ROSA-CAG-LSL-GCaMP6f mouse. Scale

bar, 10 µm. *Right*, zoomed view of the boxed region. Scale bar, 5 µm. Grey-values are photomultiplier counts. We systematically used such projections along the temporal axis to better appreciate the fine cell morphology. For the region shown, a localized, spontaneous Ca^{2+} transient occurred on frame 87. The fluorescence on the top right corner of the zoomed image corresponds to the baseline fluorescence of the soma. (B) shows the Ca^{2+} event detected on frame 87 and its zoom on a 'fire' LUT, illustrating the difficulty to outline regions of interest by simpler procedures. The asterisk shows an artifacts in the form bright and almost stationary auto-fluorescent spots resulting from lipofuscin-rich granules (10). (*C*) After baseline and outlier removal (see Methods for details), all pixels > 255 were set to 1 to prepare for the Gaussian filtering (see Methods for explanations). (*D*) In the next step, the image stack was filtered with a Gaussian filter (σ=2 pixel). Note the high baseline fluorescence of the soma (solid arrowhead). (*E*) As next step, the difference in baseline fluorescence, which makes it difficult to distinguish between Ca^{2+} events and structures with higher baseline fluorescence, was removed by subtracting the average of the first 10 frames. Note that the baseline fluorescence of the soma in the right upper corner of the zoom image (open arrowhead) disappears. (*F*) Then, a binary image was created by setting as a threshold the mean intensity of all pixels >0 of the first 10 frames plus 3 times its SD. The ROIs are delineated (area > 3 µm²). (*G*) If the Ca^{2+} event extents over several frames, only the ROI outline on the frame where the signal has its biggest area is retained (for details see online methods). In this example the Ca^{2+} signal is detectable from frame 83-89 and the ROI detected on frame 87 has the biggest area. (*H*) The mean intensity over time is extracted from the original stack (that had been processed for background and outlier removal) and normalized. The corresponding $\Delta F/F_0(t)$ trace (shown in blue) shows two Ca^{2+} peaks. However, only the 1st peak (black arrowhead) corresponds to the Ca^{2+} event detected on frame 87. The 2nd peak on the blue trace corresponds to a 2nd, spatially overlapping, Ca^{2+} event the ROI of which (shown in green) was detected on frame 102. (*I*) The $\Delta F/F_0(t)$ trace of the second, overlapping ROI (shown in green) also shows both Ca^{2+} peaks. If we would show the full-length of all $\Delta F/F_0(t)$ traces as independent traces, we would therefore count the same Ca^{2+} peak two times (or even multiple times if more than two ROIs are overlapping). Therefore, the $\Delta F/F_0$ trace was cut before and after the Ca^{2+} peak corresponding to the ROI. (*J*) When looking at the extracted the $\Delta F/F_0$ traces of an ROI, the information of the spatial extent of the Ca^{2+} event is lost. Therefore, all $\Delta F/F_0$ traces were weighed with their respective ROI's area size. For display, the $\Delta F/F_0(t)$ peaks were ordered by their (increasing) distance to the soma.

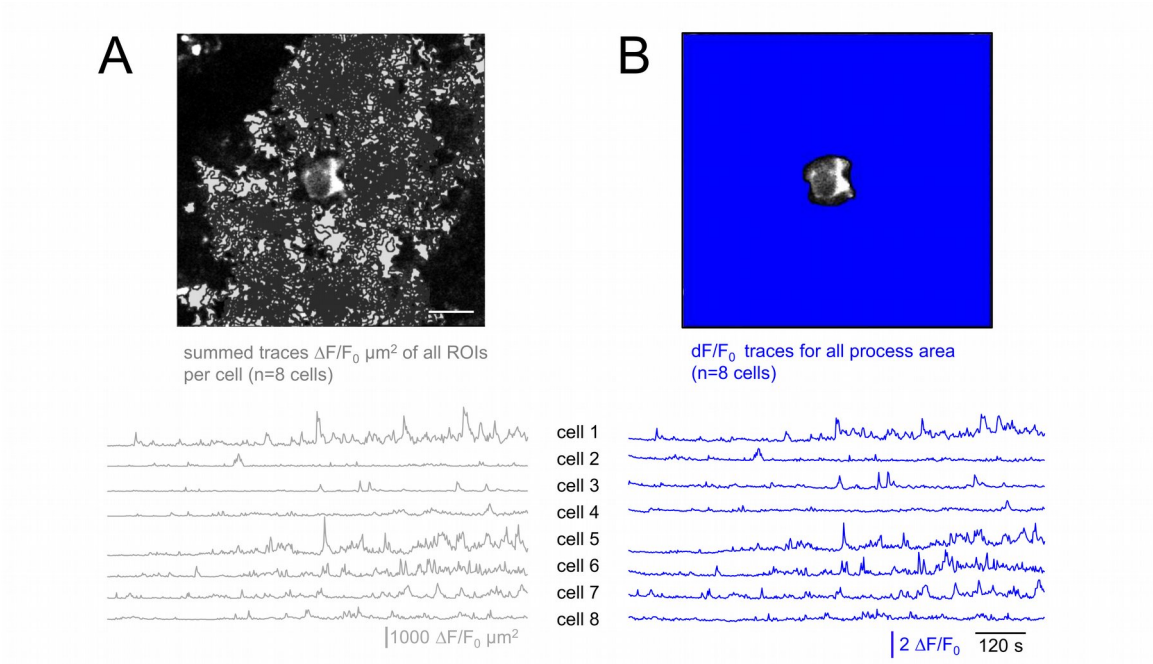

Fig. S3. Summed activity built from cumulating the weighted individually detected ROIs is equivalent to the integrated activity measured from a single large region encompassing the entire neuropil. (A) *Top*, all detected ROIs during a 500-frame recording, superimposed on the morphological overview (as in Fig. 1A) of the same cell as shown in Fig. 1 and Fig. 2. The summed activity trace is the sum of the $\Delta F/F_0(t)$ transients detected in the area of the processes (excluding the soma), multiplied, for each event, with the ROI size. Note that even if the entire cell is covered by overlaying ROIs, each ROI represents one peak at a given time, and that

asynchronous activity has been added up on the 'summed activity trace'. (c.f., Fig.1, Fig.S2 and Methods). *Bottom*, the summed activity of the cell shown above (cell 1), as well as of the other seven cells from this data set. (*B*) *Top*, the alternative, much simpler 'center-versus-surround' analysis lumps the entire process region together to one big ROI (blue). *Bottom*, the thus generated $\Delta F/F_0$ traces for the same cells as in (A) are very similar to the summed activity traces built from detected events scaled with their respective ROI size. Thus, the summed activity traces are a valid way for quantifying the overall Ca^{2+}-activity (and activation). On the other hand, at least at the signal-to-noise ratio and low background in our experiments, the much simpler centre-vs.-surround analysis is a good proxy for the ROI-based analysis, when only cumulative effects shall be studied. Scale bar, 10µm

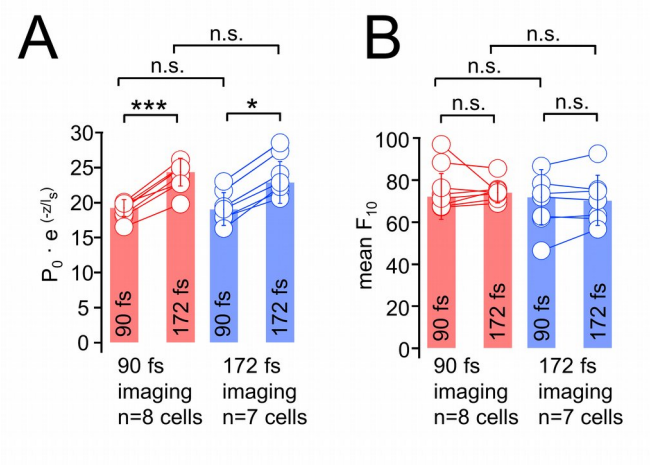

Fig. S4. Shorter pulses allow lowering the average power. (*A*) Laser powers used for 2P imaging, scaled with the imaging depth, for all cells shown in Fig. 3. Prior to imaging cells with either 90- or 172-fs pulses, we recorded 'ministacks' of ten frames with each pulse length and the average laser power was adjusted for constant 2P fluorescence (i.e., $\overline{P}^2/\tau = const.$). The power required for achieving an equal signal with 172-fs pulses was significantly higher (two sided nonparametric Wilcoxon-Mann-Whitney two-sample rank test) than for 90 fs, and there was no significant difference between the adjustment of the average laser power for both conditions (if cells were imaged with 90- or 172-fs pulses in the following recording), which means that $\overline{P}$ had been adjusted correctly. On average, we needed to increase by a factor of 1.26 ± 0.06 $\overline{P}$ when going from 90- to 172-fs pulses. (*B*) Indistinguishable baseline GCaMP6f-fluorescence measured in manually selected cell ROIs on 10-image ministacks. Bar graphs show median ± SD; *: $P < 0.05$, **: $P < 0.01$, ***: $P < 0.005$, n.s.: not significant.

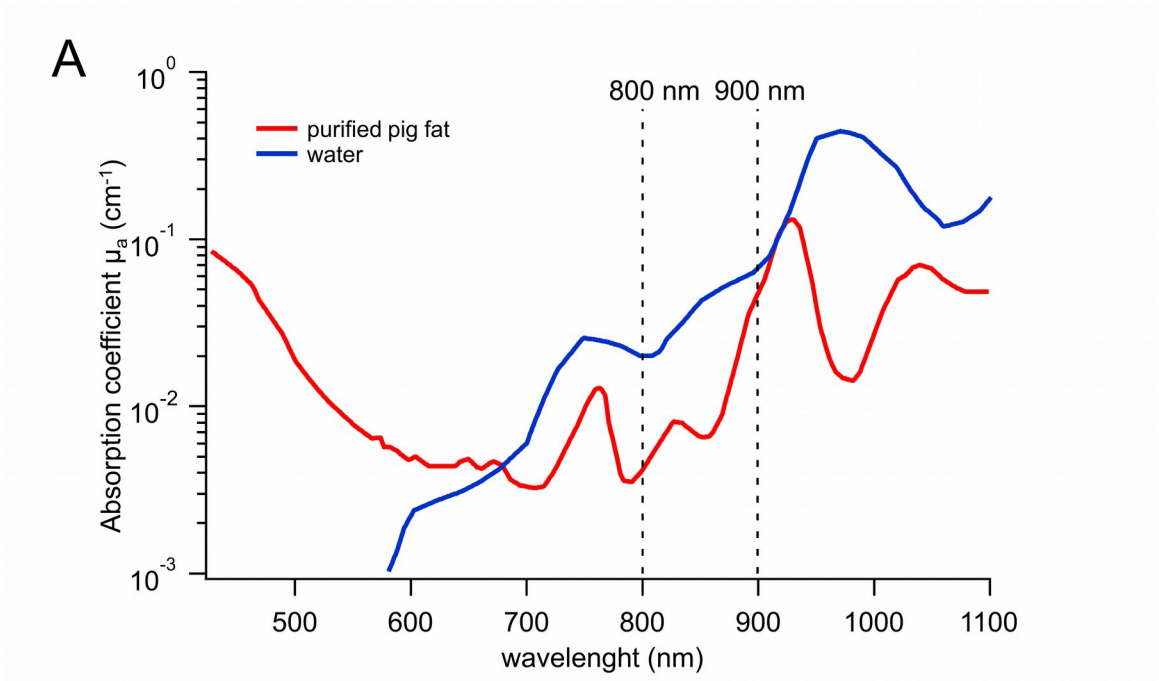

Fig. S5 Water and lipid absorption increase by more than one order of magnitude between 800 and 900 nm. Log plot of absorption coefficient μ_a vs. wavelength λ. μ_a for water (*blue*) and lipid (*red*), the main components of brain tissue, increase by more than one order of magnitude between λ < 800 nm (which have been typically been used for small-molecule chemical indicators) and λ > 900 nm, as now commonly used for imaging GECIs and light-activation of optogenetic actuators. Data from (11) (purified pig fat) and (12) (water)

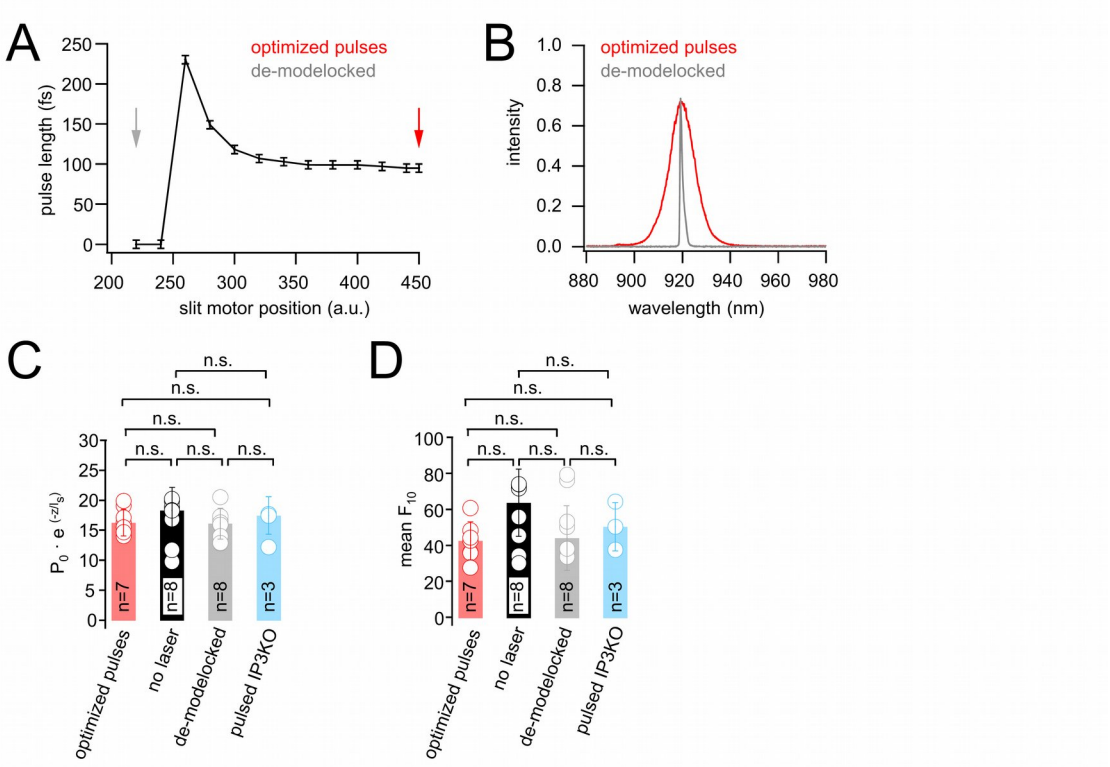

Fig. S6. CW-operation of the MaiTai laser. For de-modelocking a motorized slit aperture inside the laser cavity is partially closed under software control. (A), pulse lengths measured by autocorrelation (± 5 fs measurement error), as a function of slit motor position in arbitrary units (a.u., see Online Methods sections for details). The slit position is an internal measurement of the laser and the resulting slit diameter will differ for every laser. In our case, at 920 nm, 450 a.u. correspond to the slit motor position during normal fs-pulsed operation. For values below 350 a.u., the measured pulse length gradually increased and the laser stopped pulsing for motor positions <240 a.u.. We performed our CW experiments with a motor position of 220 a.u. (B), as expected, de-modelocking results in a reduction of the spectral width of the laser output (*red*, pulse spectrum at 90 fs; *grey*, spectrum after de-modelocking). Because only one of the blades of the slit aperture moves, the wavelength spectrum resulting when narrowing the slit is not exactly symmetrical, and the center wavelength of the pulse does not correspond to the preset command wavelength. Hence, after de-modelocking, a command wavelength of 933 nm is

necessary for a laser output centered at 920 nm. (C), Laser powers used for 2PEF imaging (normalized with the exponential power loss for imaging depth for all cells represented in Fig. 4 and Fig. 5). There is no significant difference between any of the four experimental conditions (two sided nonparametric Wilcoxon-Mann-Whitney two-sample rank test and non-parametric Kruskal-Wallis group test). (D), mean baseline fluorescence of first ten image frames is indistinguishable. Bar graphs show median ± SD; *: $P < 0.05$, **: $P < 0.01$, ***: $P < 0.005$, n.s.: not significant.

Table S1.

Antibodies, dilutions, wavelengths and filters used for immunofluorescence.

Primary antibodies	*dilution*	*species*	*supplier*	*reference*	-				
Anti-GFP	1/500	chicken	Novus-Biologicals	NB600-308	-				
Anti-S100°	1/500	rabbit	Abcam	AB52642	-				
Anti-Iba1	1/500	rabbit	Wako/Sobodia	AB5320	-				
Anti-NG2	1/500	rabbit	Millipore	019-19741	-				
Anti-NeuN	1/500	guinea pig	Millipore	ABN900	-				
Secondary antibodies					*ex*	*dic*	*em*	ZEISS set	*ref*
Anti-chicken-AlexaFluor488	1/1000	goat	Invitrogen	A-11039	BP470/40	FT495	BP525/50	eGFP shift free (HE)	38
Anti-guinea-pig-AlexaFluor546	1/1000	goat	Invitrogen	A-11074	BP545/25	FT570	BP605/70	Cy3 shift free (E)	43
Anti-rabbit-AlexaFluor546	1/1000	goat	Invitrogen	A-11035	BP545/25	FT570	BP605/70	Cy3 shift free (E)	43
DAPI					G365	FT395	BP445/50	DAPI shift free	49

Movie S1. *Spontaneous Ca^{2+} signals in a murine cortical astrocyte expressing GCaMP6f*

Diffraction-limited two-photon imaging at 0.5 Hz of an astrocyte expressing GCaMP6f in the S1 barrel cortex of an acute mouse brain slice. Analysis of this cell is shown in Fig. 1 and Fig. 2A Highly localized, spontaneous, asynchronous microdomain Ca^{2+}-signals can be seen throughout the entire neuropil. The raw-data has only been median filtered (0.5 px) after background and outlier removal (as described in the Online Methods section) and is displayed using a "fire" lookup table (LUT). The movie is superimposed on the time-averaged fluorescence (shown in grey value) over the 1st 120 frames to have visual morphological landmarks. The movie shows a 4-min recording at 25 fps (i.e., 50 times faster than original). Scale bar, 10 µm.

Movie S2. *Increase of spontaneous astrocytic Ca^{2+} signals during 2PEF imaging*

Diffraction-limited two-photon imaging at 0.5 Hz of an astrocyte expressing GCaMP6f in the S1 barrel cortex of an acute mouse brain slice as in Movie 1, but with much longer recording time (16.3 min, 500 frames). With increasing recording time, the microdomain Ca^{2+} activity in the fine processes is increasing in frequency, and an aberrant activity of the otherwise silent soma can been seen towards the end of the recording. The original data has been median filtered (0.5 px) after background and outlier removal (as described in the Online Methods section) and is shown with a "fire" LUT superimposed with a morphological image obtained by averaging the 1st 120 frames (grey scale LUT). This cell is corresponding to the one shown in the raster plot in Fig. 3A. The movie is shown at 25 fps (i.e., 50-times faster than the original). Scale bar, 10 µm.

Supplementary references

1. Denk W, Strickler JH, & Webb WW (1990) Two-photon laser scanning fluorescence microscopy. *Science* 248(4951):73-76.
2. Stosiek C, Garaschuk O, Holthoff K, & Konnerth A (2003) In vivo two-photon calcium imaging of neuronal networks. *Proc. Natl. Acad. Sci. USA* 100(12):7319-7324.
3. Helmchen F & Denk W (2005) Deep tissue two-photon microscopy. *Nat. Methods* 2(12):932-940.
4. Svoboda K & Yasuda R (2006) Principles of two-photon excitation microscopy and its applications to neuroscience. *Neuron* 50(6):823-839.
5. Mao T, O'Connor DH, Scheuss V, Nakai J, & Svoboda K (2008) Characterization and subcellular targeting of GCaMP-type genetically-encoded calcium indicators. *PloS One* 3(3):e1796.
6. Looger LL & Griesbeck O (2012) Genetically encoded neural activity indicators. *Curr. Op. Neurobiol.* 22(1):18-23.
7. Akerboom J, *et al.* (2013) Genetically encoded calcium indicators for multi-color neural activity imaging and combination with optogenetics. *Front. Mol. Neurosci.* 6.
8. Patterson GH & Piston DW (2000) Photobleaching in two-photon excitation microscopy. *Biophys. J.* 78(4):2159-2162.

9. Koester HJ, Baur D, Uhl R, & Hell SW (1999) Ca 2+ fluorescence imaging with pico-and femtosecond two-photon excitation: signal and photodamage. *Biophys. J.* 77(4):2226-2236.
10. Hopt A & Neher E (2001) Highly nonlinear photodamage in two-photon fluorescence microscopy. *Biophys. J.* 80(4):2029-2036.
11. Tan Y, Llano I, Hopt A, Würriehausen F, & Neher E (1999) Fast scanning and efficient photodetection in a simple two-photon microscope. *J. Neurosci. Meth.* 92(1):123-135.
12. Weisenburger S, Prevedel R, & Vaziri A (2017) Quantitative evaluation of two-photon calcium imaging modalities for high-speed volumetric calcium imaging in scattering brain tissue. *bioRxiv*:115659.
13. Ohkura M*, et al.* (2012) Genetically encoded green fluorescent Ca2+ indicators with improved detectability for neuronal Ca2+ signals. *PloS one* 7(12):e51286.
14. Shigetomi E, Kracun S, Sofroniew MV, & Khakh BS (2010) A genetically targeted optical sensor to monitor calcium signals in astrocyte processes. *Nat. Neurosci.* 13(6):759-766.
15. Haustein MD*, et al.* (2014) Conditions and constraints for astrocyte calcium signaling in the hippocampal mossy fiber pathway. *Neuron* 82(2):413-429.
16. Rungta RL*, et al.* (2016) Ca2+ transients in astrocyte fine processes occur via Ca2+ influx in the adult mouse hippocampus. *Glia* 64(12):2093-2103.
17. Bindocci E*, et al.* (2017) Three-dimensional Ca2+ imaging advances understanding of astrocyte biology. *Science* 356(6339):eaai8185.
18. Tian L*, et al.* (2009) Imaging neural activity in worms, flies and mice with improved GCaMP calcium indicators. *Nature Meth* 6(12):875-881.
19. Ye L, Haroon MA, Salinas A, & Paukert M (2017) Comparison of GCaMP3 and GCaMP6f for studying astrocyte Ca2+ dynamics in the awake mouse brain. *PloS One* 12(7):e0181113.
20. König K, Becker TW, I. F, Riemann I, & Halbhuber KJ (1999) Pulse-length dependence of cellular response to intense near-infrared pulses in multiphoton microscopes. *Opt. Lett.* 24:113-115.
21. Podgorski K & Ranganathan G (2016) Brain heating induced by near-infrared lasers during multiphoton microscopy. *J. Neurophysiol.* 116:1012-1023.
22. Debarre D, Olivier N, Supatto W, & Beaurepaire E (2014) Mitigating phototoxicity during multiphoton microscopy of live Drosophila embryos in the 1.0–1.2 μm wavelength range. *PLoS One* 9(8):e104250.
23. Schönle A & Hell SW (1998) Heating by absorption in the focus of an objective lens. *Opt. Lett.* 23(5):325-327.
24. Bánsághi S*, et al.* (2014) Isoform-and species-specific control of inositol 1, 4, 5-trisphosphate (IP3) receptors by reactive oxygen species. *Journal of Biological Chemistry* 289(12):8170-8181.
25. Agarwal A*, et al.* (2017) Transient opening of the mitochondrial permeability transition pore induces microdomain calcium transients in astrocyte processes. *Neuron* 93(3):587-605. e587.
26. Sherwood MW*, et al.* (2017) Astrocytic IP3Rs: Contribution to Ca2+ signalling and hippocampal LTP. *Glia* 65(3):502-513.
27. Petravicz J, Boyt KM, & McCarthy KD (2014) Astrocyte IP3R2-dependent Ca2+ signaling is not a major modulator of neuronal pathways governing behavior. *Front. Behav. Neurosci.* 8:384.

28. Srinivasan R, *et al.* (2015) Ca2+ signaling in astrocytes from Ip3r2-/-mice in brain slices and during startle responses in vivo. *Nat. Neurosci.* 18(5):708-717.
29. Sheppard CJR & Komphner R (1978) Resonant scanning optical microscope. *Appl. Opt.* 17(18):2879-2881.
30. Macias-Romero C, Zubkovs V, Wang S, & Roke S (2016) Wide-field medium-repetition-rate multiphoton microscopyreduces photodamage of living cells. *Biomed. Opt. Express* 7(4):1458-1467.
31. Liu Y, Sonek G, Berns M, & Tromberg B (1996) Physiological monitoring of optically trapped cells: assessing the effects of confinement by 1064-nm laser tweezers using microfluorometry. *Biophys. J.* 71(4):2158-2167.
32. Peterman EJ, Gittes F, & Schmidt CF (2003) Laser-induced heating in optical traps. *Biophys. J.* 84(2):1308-1316.
33. Kalmbach AS & Waters J (2012) Brain surface temperature under a craniotomy. *J. Neurophysiol.* 108(11):3138-3146.
34. Chen X, *et al.* (2012) LOTOS-based two-photon calcium imaging of dendritic spines in vivo. *Nat. Prot.* 7(10):1818.
35. Iyer V, Hoogland TM, & Saggau P (2006) Fast functional imaging of single neurons using random-access multiphoton (RAMP) microscopy. *J. Neurophysiol.* 95(1):535-545.
36. Salome R, *et al.* (2006) Ultrafast random-access scanning in two-photon microscopy using acousto-optic deflectors. *J. Neurosci. Meth.* 154(1-2):161-174.
37. Reddy GD, Kelleher K, Fink R, & Saggau P (2008) Three-dimensional random access multiphoton microscopy for functional imaging of neuronal activity. *Nat. Neurosci.* 11(6):713-720.
38. Icha J, Weber M, Waters JC, & Norden C (2017) Phototoxicity in live fluorescence microscopy, and how to avoid it. *Bioessays* 39(8).
39. Horton NG, *et al.* (2013) In vivo three-photon microscopy of subcortical structures within an intact mouse brain. *Nat. Photon.* 7(3):205.
40. Guesmi K, *et al.* (2018) Dual-color deep-tissue three-photon microscopy with a multiband infrared laser. *Light: Sci. Appl.* in press.
41. Nett WJ, Oloff SH, & Mccarthy KD (2002) Hippocampal astrocytes in situ exhibit calcium oscillations that occur independent of neuronal activity. *J. Neurophysiol.* 87(1):528-537.
42. Wang X, *et al.* (2006) Astrocytic Ca 2+ signaling evoked by sensory stimulation in vivo. *Nat. Neurosci.* 9(6):816.
43. Sun M-Y, *et al.* (2014) Astrocyte calcium microdomains are inhibited by Bafilomycin A1 and cannot be replicated by low-level Schaffer collateral stimulation in situ. *Cell Calcium* 55(1):1-16.
44. Xu H, *et al.* (2002) TRPV3 is a calcium-permeable temperature-sensitive cation channel. *Nature* 418(6894):181.
45. Xiao B, Coste B, Mathur J, & Patapoutian A (2011) Temperature-dependent STIM1 activation induces Ca2+ influx and modulates gene expression. *Nat. Chem. Biol.* 7(6):351-358.
46. Chowdhury S, Jarecki BW, & Chanda B (2014) A molecular framework for temperature-dependent gating of ion channels. *Cell* 158(5):1148-1158.
47. Shibasaki K, Ikenaka K, Tamalu F, Tominaga M, & Ishizaki Y (2014) A novel subtype of astrocytes expressing TRPV4 (transient receptor potential vanilloid 4) regulates neuronal excitability via release of gliotransmitters. *J. Cell Biol.* 289(21):14470-14480.

48. Gao X, Wu L, & O'Neil RG (2003) Temperature-modulated diversity of TRPV4 channel gating activation by physical stresses and phorbol ester derivatives through protein kinase C-dependent and-independent pathways. *J. Biol. Chem.* 278(29):27129-27137.
49. Kühn FJ, Heiner I, & Lückhoff A (2005) TRPM2: a calcium influx pathway regulated by oxidative stress and the novel second messenger ADP-ribose. *Pflügers Arch.* 451(1):212-219.
50. Xi P, Andegeko Y, Weisel LR, Lozovoy VV, & Dantus M (2008) Greater signal, increased depth, and less photobleaching in two-photon microscopy with 10 fs pulses. *Opt. Commun.* 281(7):1841-1849.
51. Pang S, Yeh AT, Wang C, & Meissner KE (2009) Beyond the 1/Tp limit: two-photon-excited fluorescence using pulses as short as sub-10-fs. *J. Biomd. Opt.* 14(5):054041.
52. Kawano H, *et al.* (2003) Attenuation of photobleaching in two-photon excitation fluorescence from green fluorescent protein with shaped excitation pulses. *Biochem. Biophys. Res. Commun.* 311(3):592-596.
53. Madisen L, *et al.* (2015) Transgenic mice for intersectional targeting of neural sensors and effectors with high specificity and performance. *Neuron* 85(5):942-958.
54. Slezak M, *et al.* (2007) Transgenic mice for conditional gene manipulation in astroglial cells. *Glia* 55(15):1565-1576.
55. Cesana E, *et al.* (2013) Granule cell ascending axon excitatory synapses onto Golgi cells implement a potent feedback circuit in the cerebellar granular layer. *J. Neurosci.* 33(30):12430-12446.
56. Ducros M, *et al.* (2011) Efficient large core fiber-based detection for multi-channel two-photon fluorescence microscopy and spectral unmixing. *J. Neurosci. Meth.* 198(2):172-180.
57. Oheim M, Beaurepaire E, Chaigneau E, Mertz J, & Charpak S (2001) Two-photon microscopy in brain tissue: parameters influencing the imaging depth. *J. Neurosci. Meth.* 111(1):29-37.
58. Schneider CA, Rasband WS, & Eliceiri KW (2012) NIH Image to ImageJ: 25 years of image analysis. *Nat. Meth.* 9(7):671.
59. Rueden CT, *et al.* (2017) ImageJ2: ImageJ for the next generation of scientific image data. *BMC bioinformatics* 18(1):529.
60. Schindelin J, *et al.* (2012) Fiji: an open-source platform for biological-image analysis. *Nat. Meth.* 9(7):676.
61. Bethge P, *et al.* (2017) An R-CaMP1. 07 reporter mouse for cell-type-specific expression of a sensitive red fluorescent calcium indicator. *PloS one* 12(6):e0179460.
62. Van Veen R, *et al.* (2005) Determination of visible near-IR absorption coefficients of mammalian fat using time-and spatially resolved diffuse reflectance and transmission spectroscopy. *J. Biomed. Opt.* 10(5):054004.
63. Chung S, *et al.* (2008) In vivo water state measurements in breast cancer using broadband diffuse optical spectroscopy. *Physics Med. Biol.* 53(23):6713.